The three-dimensional generalized Hénon map: Bifurcations and attractors •

Cite as: Chaos **32**, 113127 (2022); https://doi.org/10.1063/5.0103436 Submitted: 15 June 2022 • Accepted: 24 October 2022 • Published Online: 09 November 2022

🗓 Amanda E. Hampton and 匝 James D. Meiss

COLLECTIONS

This paper was selected as Featured









APL Machine Learning

Machine Learning for Applied Physics Applied Physics for Machine Learning

Now Open for Submissions



The three-dimensional generalized Hénon map: Bifurcations and attractors •

Cite as: Chaos **32**, 113127 (2022); doi: 10.1063/5.0103436 Submitted: 15 June 2022 · Accepted: 24 October 2022 · Published Online: 9 November 2022







Amanda E. Hampton^{a)} and James D. Meiss^{b)}





AFFILIATIONS

Department of Applied Mathematics, University of Colorado Boulder, Boulder, Colorado 80309-0526, USA

- ^{a)}Author to whom correspondence should be addressed: Amanda.Hampton@colorado.edu
- b) Electronic mail: James. Meiss@colorado.edu

ABSTRACT

We study dynamics of a generic quadratic diffeomorphism, a 3D generalization of the planar Hénon map. Focusing on the dissipative, orientation preserving case, we give a comprehensive parameter study of codimension-one and two bifurcations. Periodic orbits, born at resonant, Neimark-Sacker bifurcations, give rise to Arnold tongues in parameter space. Aperiodic attractors include invariant circles and chaotic orbits; these are distinguished by rotation number and Lyapunov exponents. Chaotic orbits include Hénon-like and Lorenz-like attractors, which can arise from period-doubling cascades, and those born from the destruction of invariant circles. The latter lie on paraboloids near the local unstable manifold of a fixed point.

Published under an exclusive license by AIP Publishing. https://doi.org/10.1063/5.0103436

Since Hénon's observation of strange, chaotic attractors in his eponymous two-dimensional map, this quadratic map has become a pivotal model to understand chaotic dynamics in the plane.^{2,3} It is of much interest to understand the dynamics of higher-dimensional generalizations of this map as models for the onset and development of chaotic dynamics. As a prototypical model, we study the so-called 3D generalized Hénon map,4 which is a quadratic normal form for several bifurcation scenarios. Building upon previous work, we study the periodic and aperiodic dynamics of this map using a variety of visualizations in both parameter and phase space. For example, Arnold tongues, or resonant regions, in parameter space correspond to attracting periodic orbits in phase space. We compute heteroclinic trajectories between orbits in the tongues as well as in period-doubling cascades. We also follow the evolution of invariant circles as they bifurcate, some of which can become complex chaotic attractors.

I. INTRODUCTION

The two-dimensional Hénon map¹ is the quadratic diffeomorphism of the plane: every such diffeomorphism is conjugate to a map in the two-parameter Hénon family. Prominent rigorous results for this diffeomorphism include that of Devaney and Nitecki,5 who showed that the dynamics of its bounded orbits are conjugate to a

Smale horseshoe in some parameter regimes, and that of Benedicks and Carleson,6 who showed that when the Jacobian is sufficiently small, there are cases for which the map has a transitive attractor with a positive Lyapunov exponent. It was also shown that the horseshoe in this map can be thought of as arising from an anti-integrable limit, where the dynamics becomes non-deterministic.7

Some of these results have been generalized to higherdimensional maps. For the three-dimensional (3D) case, it was shown in Ref. 8 that every quadratic diffeomorphism with a quadratic inverse is conjugate to the map $L: \mathbb{R}^3 \to \mathbb{R}^3$,

$$L(x, y, z) = (\delta z + G(x, y), x, y),$$

$$G(x, y) = \alpha + \tau x - \sigma y + ax^2 + bxy + cy^2.$$
(1)

This analysis was later generalized to include 3D quadratic diffeomorphisms that have quartic inverses9 and to higher dimensions.10 The diffeomorphism (1) arises as a normal form in the volumepreserving ($\delta = 1$) case near a fixed point with three unit multipliers. 11,12 It has also been shown to be a normal form near a map with a saddle-focus fixed point that has a quadratic homoclinic tangency. 4,13 The theory of anti-integrability also applies to these maps when $\alpha \to -\infty$; see, e.g., Ref. 14.

The map L has seven parameters, six in the quadratic polynomial G and $\delta = \det DL$, the Jacobian determinant. This parameter set can be reduced, as noted in Ref. 8: whenever $a + b + c \neq 0$ and

 $2a+b\neq 0$ (if one of these is violated, other scaling transformations can be found to eliminate two of the parameters), an affine coordinate transformation allows one to set

$$a + b + c = 1$$
 and $\tau = 0$. (2)

Using this simplification, (1) depends only on (α, σ, a, c) and the Iacobian δ .

The case (a, b, c) = (1, 0, 0) has been called "the 3D Hénon map" since it only has one nonlinear term similar to the classical Hénon map.1 In a series of papers starting with Refs. 4 and 13, Gonchenko and collaborators focus on the formation of chaotic attractors for this map (in their notation, $M_1 = -\alpha$, $B = \delta, M_2 = -\sigma$). These attractors are shown to be "wild hyperbolic" (nearby maps have Newhouse tangencies between stable and unstable manifolds¹⁵) near the parameters $(\alpha, \sigma, \delta) = (\frac{1}{4}, -1, 1)$, where a pair of fixed points are born with multipliers (-1, -1, 1). These attractors are also "pseudo-hyperbolic" (its tangent space splits into a strong stable subspace and a complementary subspace that exponentially expands volume), such as like the Lorenz attractor, implying that every orbit in the attractor has at least one positive and one negative Lyapunov exponent. According to Ref. 16, there are five types of such attractors formed from the unstable manifold of a fixed point, including "Lorenz-like" and several "figure-eight" attractors.¹⁷ Moreover, there are infinite cascades in the parameter space of nearby systems with Lorenz-like attractors. 18 Chaotic attractors for the non-orientable case have also been studied.¹⁹

Following Gonchenko *et al.*, we will primarily study the 3D Hénon case using the scaling (2) and taking $0 < \delta < 1$ so that the map is volume contracting and orientation preserving. We focus on two examples:

- (SC) Strongly Contracting: $(a, c, \delta) = (1, 0, 0.05)$,
- (MC) Moderately Contacting: $(a, c, \delta) = (1, 0, 0.7)$,

allowing (α,σ) to vary. In Sec. II, we recall basic bifurcation behavior of periodic orbits for a 3D map using the trace and second trace of the Jacobian. These bifurcation conditions are transformed to conditions on (α,σ) for the fixed points of (1) in Sec. III. A similar bifurcation criterion was obtained for the 3D Hénon map in Ref. 20 for the case that $\sigma=\delta$, as well as in Ref. 21 when $\sigma=0$ for three and more dimensions. In Sec. IV, we prove that all bounded orbits of the 3D Hénon map lie within a finite cube about origin, following the proof of a related theorem in Ref. 8.

The simplest bounded orbits are stable and periodic. Parameter regions in the (α, σ) -plane containing such attractors, analogous to Arnold tongues, are computed in Sec. V, where we also compute heteroclinic manifolds between stable and unstable orbits. In Sec. VI, we study aperiodic attractors, computing the maximal Lyapunov exponent to distinguish between regular and chaotic cases. Regular aperiodic attractors come in the form of invariant circles, which we study in Sec. VI A expanding upon the volume-preserving case studied in Ref. 12. In Sec. VI B, we find Hénon-like attractors for case (SC) and discrete, Lorenz-like attractors 22 for case (MC). Additionally, we observe chaotic attractors arising from bifurcations of invariant circles that are unlike those in Refs. 23 and 24; these also do not seem to be related to the generalizations of Smale's horseshoe to 3D found by Ref. 25.

II. BIFURCATIONS FOR 3D MAPS

For a fixed point $\xi^* = f(\xi^*)$ of a 3D map f, the eigenvalues of the Jacobian $A = Df(\xi^*)$ are given by the zeros of a characteristic polynomial,

$$p_A(\lambda) = \det(\lambda I - A) = \lambda^3 - t\lambda^2 + s\lambda - d. \tag{3}$$

We refer to these as the *multipliers* of the fixed point. Here, $t = \operatorname{tr}(A)$ is the trace and $d = \det(A)$. An expression for the "second trace," s, can be obtained from the Cayley–Hamilton theorem: a matrix satisfies its own characteristic polynomial, $A^3 - tA^2 + sA - dI = 0$. Multiplying this by A^{-3} implies that $s = d\operatorname{tr}(A^{-1})$. Finally, multiplying the Cayley polynomial by A^{-1} and taking the trace gives

$$s = \frac{1}{2} (t^2 - \operatorname{tr}(A^2)).$$
 (4)

Of course, the multipliers can be related to the coefficients of (3) by the symmetric polynomials,

$$t = \lambda_1 + \lambda_2 + \lambda_3,$$

$$s = \lambda_1 \lambda_2 + \lambda_1 \lambda_3 + \lambda_2 \lambda_3,$$

$$d = \lambda_1 \lambda_2 \lambda_3.$$
(5)

More generally, for an orbit, $\xi_t = f(\xi_{t-1})$, that has period n, $\xi_0 = f^n(\xi_0)$, the Jacobian becomes

$$A = Df^{n}(\xi_{0}) = Df(\xi_{n-1})Df(\xi_{n-2}), \dots, Df(\xi_{1})Df(\xi_{0}).$$

Thus, using the same process as above, we can find a general expression for the trace and second trace of a period-*n* orbit,

$$t = \operatorname{Tr}(Df^n), \quad s = \frac{1}{2} \left(t^2 - \operatorname{Tr}\left((Df^n)^2 \right) \right).$$

Following Ref. 26, the simplest, local codimension-one bifurcations—saddle-node, period-doubling, and Neimark–Sacker—occur when at least one multiplier has unit modulus. Each of these occurs on a surface in (t, s, d), given in Table I. Sections through these surfaces for four values of d are shown in Fig. 1; similar figures can be found in Ref. 8 for the case d=1 and in Ref. 16, where they are referred to as "saddle-charts."

Saddle-node (SN) bifurcations require a unit multiplier so that (3) gives $p_A(1) = 1 - t + s - d = 0$. This corresponds to a line in the (t,s)-plane, shown in blue in Fig. 1. A period-doubling (PD) bifurcation occurs when there is a -1 multiplier or $p_A(-1) = -1 - t - s - d = 0$, shown in red in Fig. 1. The third codimension-one bifurcation, the Neimark–Sacker (NS), occurs when there is a pair of complex multipliers with a unit modulus; it generically results in the creation of an invariant circle or a pair of periodic orbits with differing stabilities. Since $|\lambda_{1,2}| = 1$, (5) gives $\lambda_3 = d$ so that $p_A(d) = d(d^2 - td + s - 1) = 0$. The resulting line, s = d(t - d) + 1, is shown in black in Fig. 1. Solving for the complex multipliers gives

$$\lambda_{1,2} = e^{\pm 2\pi i \omega} = \frac{1}{2} \left(t - d \pm \sqrt{(t - d)^2 - 4} \right)$$
 (6)

or that $t - d = 2\cos(2\pi\omega)$ for rotation number ω .

Some codimension-two bifurcations occur along the NS line when $\omega = \frac{p}{q}$ and generically result in the birth of a pair of period-q orbits. The end points of the NS line occur where it intersects the

TABLE I. Local bifurcations for a 3D map with Jacobian d, trace t, and second trace s. For each d, codimension-one bifurcations lie on lines in the (t, s) plane and codimension-two bifurcations at points. Since $\lambda_1\lambda_2\lambda_3=d$, for the NS and resonant bifurcations, $\lambda_3=d$, and for SNf, $\lambda_3=-d$.

CoD	Bifurcation	L	Multiplier	(t, s)
1	Saddle-node Period-doubling Neimark–Sacker	(SN) (PD) (NS)	$\lambda_1 = 1$ $\lambda_1 = -1$ $\lambda_{1,2} = e^{\pm 2\pi i \omega}$	$(t, t+d-1) (t, -t-d-1) (d+2\cos(2\pi\omega), 2d\cos(2\pi\omega)+1)$
2	$\omega = \frac{0}{1}$ $\omega = \frac{1}{2}$ $\omega = \frac{1}{3}$ $\omega = \frac{1}{4}$ Saddle-node flip	(R1) (R2) (R3) (R4) (SNf)	$\lambda_{1,2} = 1$ $\lambda_{1,2} = -1$ $\lambda_{1,2} = e^{\pm 2\pi i/3}$ $\lambda_{1,2} = \pm i$ $\lambda_{1} = 1, \lambda_{2} = -1$	(d+2, 2d+1) $(d-2, 1-2d)$ $(d-1, 1-d)$ $(d, 1)$ $(-d, -1)$

SN and PD lines at $\omega=0$ and $\omega=\frac{1}{2}$, labeled (R1) and (R2), respectively, in Table I. The table also shows the period-three (R3) and period-four (R4) cases. Finally, the saddle-node flip (SNf) bifurcation point, with multipliers (-1,1,-d), is at the intersection of the PD and SN lines.

A curve in parameter space along which there is a double multiplier, say $\lambda_1=\lambda_2=r$, for $r\in\mathbb{R}$, corresponds to the transition from real to complex multipliers. Using (5), this occurs when $\lambda_3=d/r^2$ along the parametric curve

$$(t,s) = \left(\frac{d}{r^2} + 2r, 2\frac{d}{r} + r^2\right). \tag{7}$$

This curve has two branches when $d \neq 0$, one of which has a cusp at $r^3 = d$, i.e., at $(t,s) = 3(d^{1/3},d^{2/3})$. When r = 1, this curve is tangent to the SN line and crosses the R1 point, and when r = -1, the curve is tangent to the PD line and crosses the R2 point. Four segments of these curves, labeled by ranges of the double multiplier, are shown in Fig. 1.

We also include representative configurations of the multipliers in the complex plane relative to the unit circle for each region of the (t,s) plane in Fig. 1. For $0 \le d < 1$, there exists a small triangular region with all stable multipliers $(|\lambda_i| < 1)$ that is bounded by the SN, PD, and NS lines with vertices R1, R2, and SNf. Otherwise, the SN and PD lines divide the plane into four regions where stability types of the multipliers of the fixed points alternate between having one unstable and two stable multipliers and two unstable and one stable multiplier.

III. FIXED POINTS OF THE QUADRATIC MAP

We now apply the results of Sec. II to fixed points of (1) with parameter convention (2). The fixed points have the form $\xi_{\pm} = (x_{\pm}, x_{\pm}, x_{\pm})$, where

$$x_{\pm} = \frac{1}{2} (\sigma - \delta + 1) \pm \sqrt{\alpha_{SN} - \alpha},$$

$$\alpha_{SN} \equiv \frac{1}{4} (\sigma - \delta + 1)^{2},$$
(8)

provided $\alpha \leq \alpha_{SN}$. These are born in a saddle-node bifurcation when $\alpha = \alpha_{SN}$ with $x_{\pm}^2 = x_{SN}^2 = \alpha_{SN}$. Thinking of α as a bifurcation parameter, the form (8) implies that there is a fixed point at x^* , say, when $\alpha = \alpha^* \leq \alpha_{SN}$ whenever $(x^* - x_{SN})^2 = \alpha_{SN} - \alpha^*$ or,

equivalently, when

$$\alpha^* = x^* (2x_{SN} - x^*). (9)$$

The stability of the fixed points is determined by the linearization of (1),

$$DL = \begin{pmatrix} 2ax + by & -\sigma + bx + 2cy & \delta \\ 1 & 0 & 0 \\ 0 & 1 & 0 \end{pmatrix}.$$

This is in a companion form, implying that at a fixed point, the trace and second trace are

$$t_{\pm} = (2a + b)x_{\pm}, \quad s_{\pm} = \sigma - (b + 2c)x_{\pm},$$
 (10)

and the Jacobian is $d = \delta$.

The fixed points lie on a line in the (t, s)-plane that can be found by eliminating x_{\pm} and b from (10),

$$(1+a-c)(s_{\pm}-\sigma) = -(1-a+c)t_{\pm}, \tag{11}$$

and are born at the intersection of this line with the SN line from Table I,

$$t_{SN} = \frac{1}{2}(\sigma - \delta + 1)(1 + a - c).$$

Moreover, (10) gives

$$s_{\pm} - t_{\pm} - \delta + 1 = \sigma - \delta + 1 - 2x_{\pm} = \mp 2\sqrt{\alpha_{SN} - \alpha}$$
.

Since $x_- < x_{SN} < x_+$, this implies that x_+ lies below and x_- above the SN line in the (t,s) plane. Therefore, when $0 \le \delta < 1$, if there exists an attracting fixed point, it must be ξ_- .

Using the equations for the SN and PD lines in Table I, the fixed points are born above the PD line when $t_{SN} > -\delta$ or

$$(\delta-\sigma-1)(1+a-c)<2\delta.$$

Provided $a \neq c$, one of the fixed points undergoes a period-doubling bifurcation at

$$x_{PD} = \frac{\sigma + \delta + 1}{2(c - a)}. (12)$$

An expression for the period-doubling value of α is obtained from (9): $\alpha_{PD} = x_{PD}(2x_{SN} - x_{PD})$. Note that for a fixed point to "double," it needs to exist; thus, we must have $\alpha_{PD} \leq \alpha_{SN}$. In addition, when

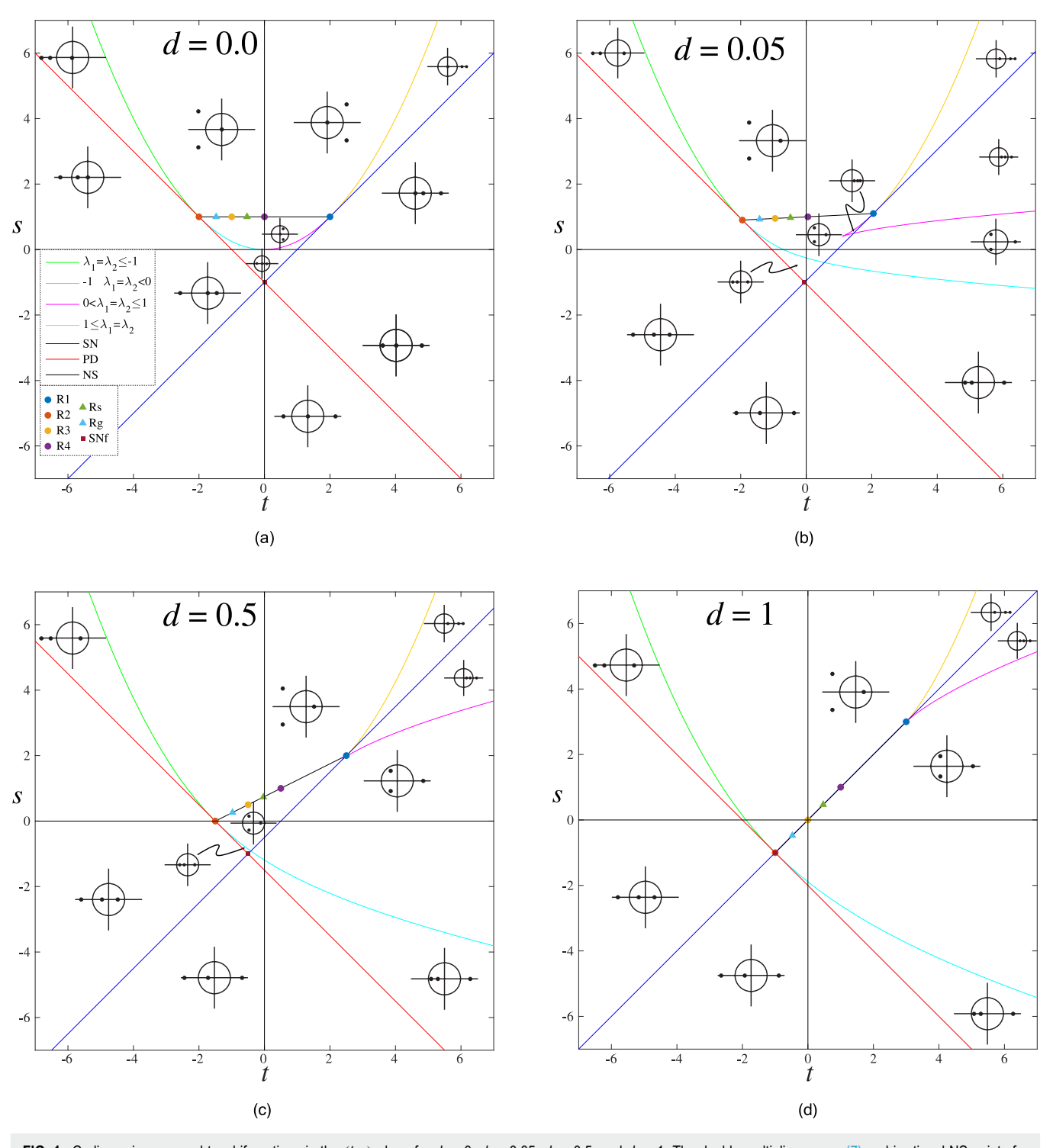


FIG. 1. Codimension-one and two bifurcations in the (t,s)-plane for d=0, d=0.05, d=0.5, and d=1. The double-multiplier curves (7) and irrational NS points for $\omega=(\sqrt{5}-1)/2$ (Rg) and $\omega=1/\sqrt{2}$ (Rs) for the golden and silver means, respectively, are also shown. Behavior at irrational points along the NS line will be discussed in Sec. VI. The insets show the complex plane with representative multiplier locations relative to the unit circle.

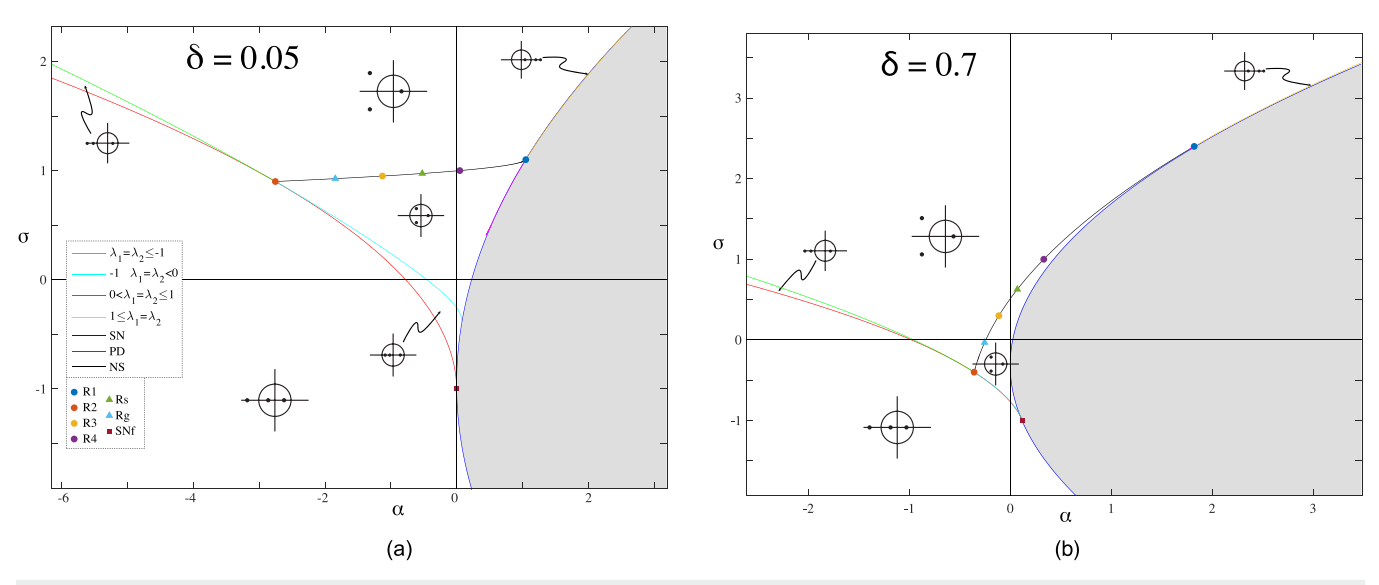


FIG. 2. Bifurcation curves for the fixed point ξ_- of (1) for the case (SC) ($\delta=0.05$) and (MC) ($\delta=0.7$) as (α,σ) vary. The fixed points do not exist to the right of the SN line, i.e., in the gray region. The double-multiplier curves (7) are shown for $|r| > \sqrt{\delta}$, as this range corresponds to a double multiplier for ξ_- ; see the Appendix for details.

 $x_{PD} < x_{SN}$, the ξ_- fixed point doubles, and when $x_{PD} > x_{SN}$, the ξ_+ point doubles.

Similarly, using (10) and the expression in Table I for the NS bifurcation gives

$$x_{NS} = \frac{\sigma - \delta\tau + \delta^2 - 1}{\delta(1 + a - c) + (1 - a + c)},$$
(13)

provided the denominator is nonzero. Of course, this bifurcation only exists if the fixed points intersect the NS line on the interval $\delta-2 < t < \delta+2$. Again, (9) can be used to determine the bifurcation value, α_{NS} .

When the parameters (a, c, δ) are fixed, the generic bifurcation diagrams of Fig. 1 can be transformed to corresponding diagrams for a fixed point in the (α, σ) plane; details are given in the Appendix, including criteria for codimension-two bifurcations. The results are shown in Fig. 2 for the fixed point ξ_- as this is the only fixed point that can be attracting—for cases (SC) and (MC).

IV. BOUNDED ORBITS

In Ref. 8, it was shown that if the quadratic form $Q(x, y) = ax^2 + bxy + cy^2$ is positive definite and $\delta = 1$, then there is a cube that contains all bounded orbits of (1); equivalently, all points outside of this cube escape to infinity. We show in this section that a similar argument can be used for the case (a, b, c) = (1, 0, 0), where Q is semi-definite, for any $\delta > 0$.

Lemma 1. If (a,b,c)=(1,0,0), $\tau=0$, and $\delta>0$, then all bounded orbits of the map (1) are contained within the cube $\{(x,y,z):|x|,|y|,|z|\leq\kappa\}$ where

$$\kappa = \frac{1}{2} \left(|\sigma| + \delta + 1 + \sqrt{(|\sigma| + \delta + 1)^2 + 4|\alpha|} \right). \tag{14}$$

Proof. For an orbit $\xi_t = (x_t, y_t, z_t)$ of the map (1), $y_t = x_{t-1}$ and $z_t = x_{t-2}$; therefore, the map is equivalent to the forward and backward difference equations,

$$x_{t+1} = \delta x_{t-2} + \alpha - \sigma x_{t-1} + x_t^2, \tag{15}$$

$$x_{t-3} = \delta^{-1} \left(x_t - \alpha + \sigma x_{t-2} - x_{t-1}^2 \right). \tag{16}$$

There are three cases to consider that depend on which term in the sequence x_{t-2}, x_{t-1}, x_t is the largest.

1. $|x_t| \ge \max(|x_{t-1}|, |x_{t-2}|)$: then, (15) gives

$$x_{t+1} \ge x_t^2 - (|\sigma| + |\delta|)|x_t| - |\alpha|,$$

giving a lower bound to the forward iterate. Notice this inequality implies that the next iterate lies above an even, piecewise-parabolic curve with a negative vertical intercept. Thus, there exists $\kappa > 0$ such that whenever $|x_t| > \kappa$, we have

$$x_{t+1} \ge x_t^2 - (|\sigma| + |\delta|)|x_t| - |\alpha| > |x_t| > \kappa.$$

Here, κ is the maximum root of $x_t^2 - (|\sigma| + |\delta| + 1)|x_t| - |\alpha|$, given by (14). This implies that $x_{t+1} > |x_t| \ge |x_{t-1}|$. Recursively applying this argument to each forward step implies that

$$x_{t+k} > x_{t+k-1} > \cdots > x_{t+1} > |x_t| > \kappa$$
.

This is a monotone increasing sequence that cannot have a finite limit: if it were to converge, it would have to converge to one of the fixed points x_{\pm} , (8), but this is impossible since, by simple calculation, $\kappa > |x_{\pm}|$.

2. $|x_{t-2}| \ge \max(|x_t|, |x_{t-1}|)$: then, (16) gives

$$x_{t-3} \le \delta^{-1} \left(-x_{t-2}^2 + (1+|\sigma|)|x_{t-2}| + |\alpha| \right),$$

giving an upper bound to the preimage. This inequality is the space below an even, downward facing piecewise parabola with

a positive vertical intercept. As before, when $|x_{t-2}| > \kappa$,

$$x_{t-3} \le \delta^{-1} \left(-x_{t-2}^2 + (1+|\sigma|) |x_{t-2}| + |\alpha| \right) < -|x_{t-2}| < -\kappa.$$

Applying this argument recursively implies that x_{t-k} is a monotone decreasing sequence. Again, the sequence must be unbounded.

3. $|x_{t-1}| \ge \max(|x_t|, |x_{t-2}|)$: using (16) gives

$$x_{t-3} \le \delta^{-1} \left(-x_{t-1}^2 + (1+|\sigma|)|x_{t-1}| + |\alpha| \right) < -|x_{t-1}|$$

whenever $-|x_{t-1}| < -\kappa$. Recursively, this implies $x_{t-3} < -|x_{t-1}| \le -|x_{t-2}|$, resulting in the same scenario as (2).

Thus, bounded orbits of the map (1) with $(a, b, c) = (1, 0, 0), \tau = 0$, and $\delta > 0$ must lie within a κ -cube about the origin.

To illustrate this result, we compute the volume of bounded orbits, i.e., the volume of the basin of any attractors, for the cases (SC) and (MC); see Fig. 3. For each point on a 500^2 grid in the (α, σ) -plane for which the fixed points (8) exist $(\alpha \le \alpha_{SN})$, we choose 50^3 initial conditions on a uniform grid in a cube with bounds (14) that vary with (α, σ) . An orbit is declared to be unbounded if it leaves the κ -cube within 200 iterates.

The selected parameters in Fig. 3 focus on the triangular regions of Fig. 2 where ξ_- is an attracting fixed point. The bifurcation curves (dashed) and codimension-two points are also shown (refer to the legend in Fig. 2). Note that near the SN line, the volume of bounded orbits in the κ -cube is small since most are found near the fixed points, which are close together.

V. PERIODIC ATTRACTORS

In this section, we compute regions in parameter space for which (1) has attracting periodic orbits. If there is a unique, bounded attractor, it can easily be found by choosing an appropriate initial condition within the cube of Lemma 1 and iterating until the orbit limits on the attractor. Once the transient is removed, parameter regions of periodic behavior can be computed by looking for recurrence.

Computed periodic regions are shown in Fig. 4 for the two cases, (SC) and (MC). To compute these, the initial point is set to $\xi_0=0$ when neither of the fixed points exist [i.e., to the right of the SN line in the (α,σ) -plane] or to $\xi_0=\xi_-+(0.001,0,0)$, near the fixed point. For each (α,σ) on a 1000^2 grid, the map (1) is iterated T=5000 times to eliminate transients. The orbit is declared to diverge (white region) if $|\xi_t|>\kappa_{max}$ for some $t\leq T$, where κ_{max} is the maximum of (14) over the studied parameter region $[\kappa_{max}=3.237$ for (SC) and 4.632 for (MC)]. Otherwise, the point ξ_T is iterated up to 90 more steps, checking for return time, defined as the first time, p, for which the distance

$$\|\xi_{T+p} - \xi_T\| < 10^{-4}. (17)$$

Thus, we find approximately periodic orbits up to period 90; the period p is indicated by the color map in Fig. 4. If an orbit is not periodic by this definition, the point is colored black or gray; we will discuss the dynamics in these regions in Sec. VI.

Note that the initial condition, the number of transient iterations, recurrence tolerance, and grid size were strategically chosen to provide sufficient detail at the pictured resolution but still lessen the

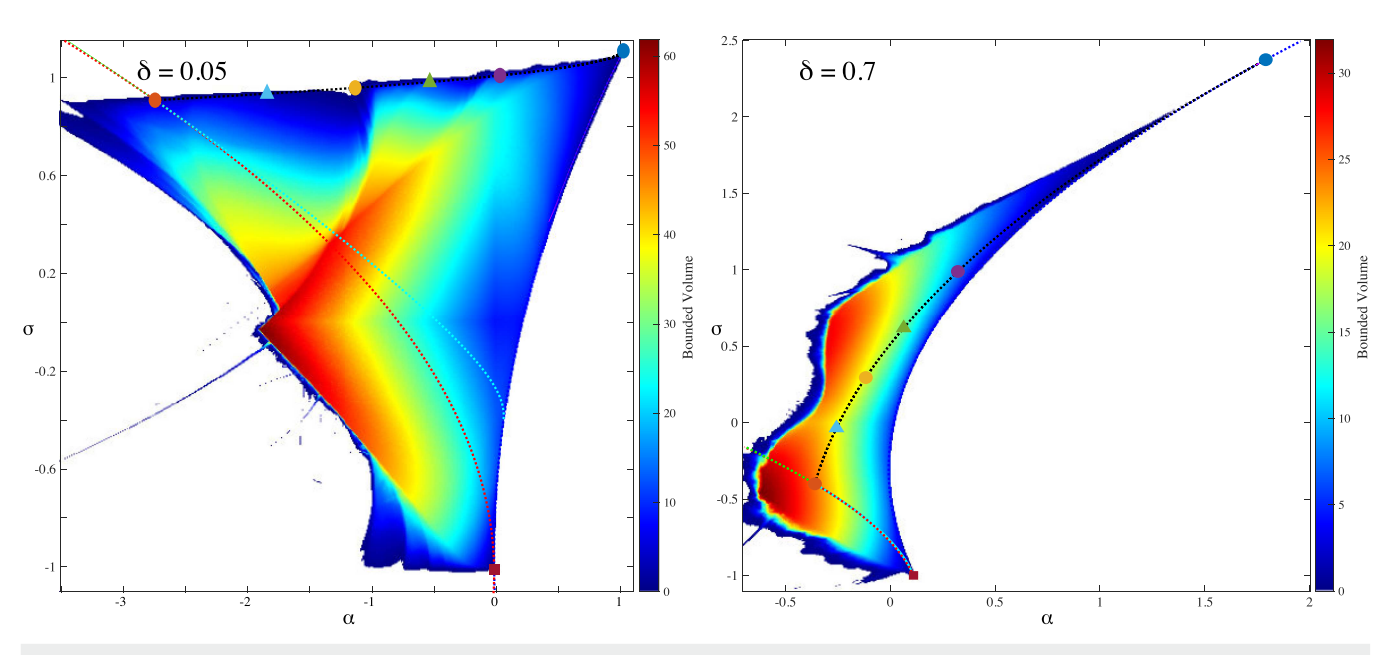


FIG. 3. The volume of bounded orbits for 50^3 initial conditions in the κ -cube for case (SC) ($\delta=0.05$) and case (MC) ($\delta=0.7$) as a function of (α,σ). Bifurcation curves and points from Fig. 2 are also shown. Notice the color bar for case (SC) includes larger values, with a maximum volume of 61.8. This is expected as it is more strongly contracting than case (MC), which has a maximum volume of 31.9.

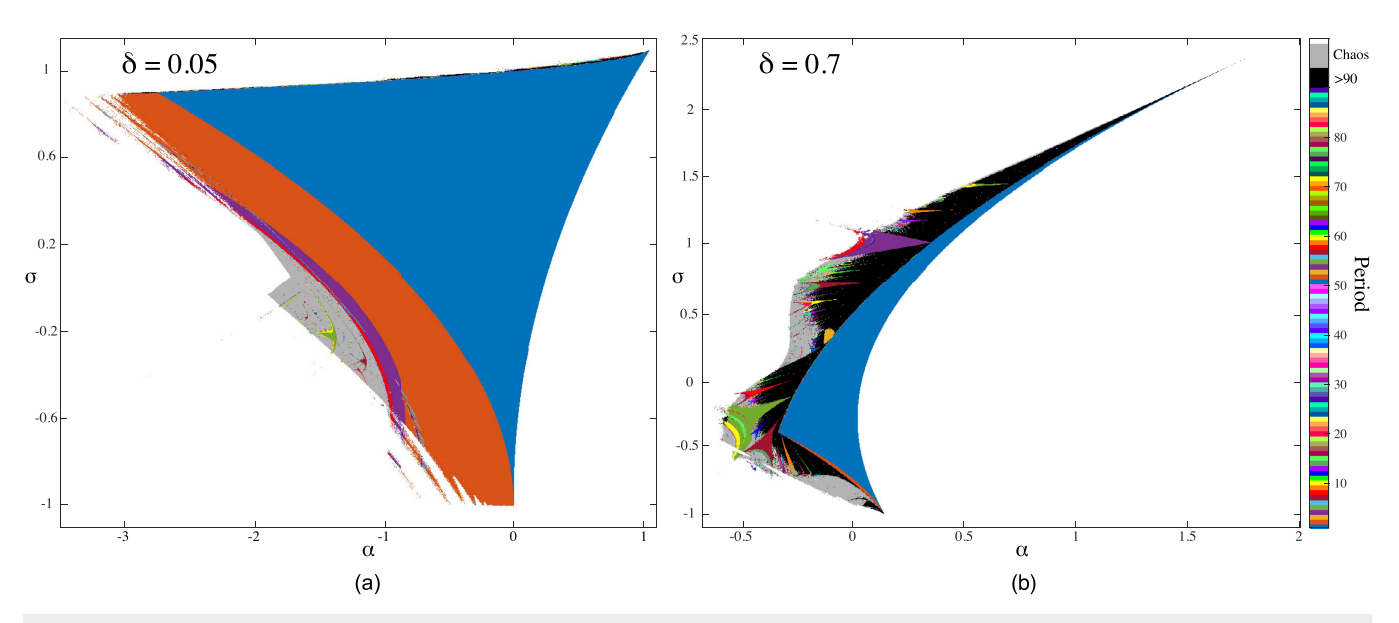


FIG. 4. Parameter dependence of the dynamics of (1) for (a) (SC) and (b) (MC) as (α, σ) vary. The white region corresponds to orbits that diverge. Bounded, periodic attractors, for periods up to 90, are colored as shown in the color bar. The black region corresponds to period >90 or aperiodic, regular behavior, and the gray region to chaotic orbits, i.e., where the maximal Lyapunov exponent $\mu_T > \mu_0 = 0.0003$; see Sec. VI.

computational expense. Clearly, computations of precise bifurcation boundaries would require more stringent tolerances.

Since this method uses a single initial condition, it cannot find cases where there are multiple attractors. Additionally, it is possible that the chosen initial condition leads to an unbounded orbit when there is still an attractor somewhere in the κ -cube. Nevertheless, for almost all (α, σ) points that have bounded orbits in Fig. 3, the orbit iterated in Fig. 4 is also bounded; therefore, with a few exceptions, it does not appear that the orbit of ξ_0 is unbounded when there are other bounded orbits. We plan to discuss such exceptional cases and the case of multiple attractors in future papers.

The largest, blue regions in Fig. 4 correspond to period-one, where ξ_- is attracting. This region is bounded by the SN, PD, and NS curves seen in Fig. 2. When the fixed point loses stability at the PD curve, an attracting period-two orbit is born; the period-two (vivid orange) region is prominent in Fig. 4(a), though there is also a thin period-two region just below the PD curve in Fig. 4(b). Period-doubling bifurcations leading to period-four (magenta) and eight (red) are also seen in Fig. 4(a). By contrast, in Fig. 4(b), the period-two orbit in (MC) looses stability by a NS bifurcation; therefore, a doubling cascade is not seen in this case.

Resonant "tongues," analogous to the Arnold tongues found in circle maps, start along the NS curve where ω is rational; these are prominent in Fig. 4(b). Especially visible are the $\omega=\frac{1}{3}$ (yellow), $\frac{1}{4}$ (magenta), $\frac{2}{5}$ (dark green), and $\frac{3}{7}$ (brown) tongues. Bifurcation points along the NS curve for the first two of these were indicated in Fig. 2 as R3 and R4.

Enlargements of case (SC), shown in Fig. 5, and of case (MC), Fig. 7, provide more detail. In Subsections V A and V B, we show

a few examples of the corresponding orbits in phase space for the period-doubling cascade and resonant tongues.

A. Period-doubling cascade

A supercritical period-doubling bifurcation generically occurs when a real multiplier of an attracting periodic orbit passes through -1, the PD line of Fig. 1, and results in the creation of a stable orbit of twice the period. As is well known from studies of 1D maps, this behavior often recurs, resulting in a cascade of doubling bifurcations that accumulates leading to the formation of a chaotic attractor.^{2,3} Such a cascade is prominent in case (SC) seen in Fig. 4(a) and its enlargement Fig. 5. Cascades are also often seen at the ends of the resonant tongues; most apparent for case (MC) in Fig. 7, which shows a multitude of tongues radiating from the attracting fixed point region.

To visualize the progression of the period-doubling cascade in case (SC), we fix $\sigma \approx -0.291$ along the line segment shown in Fig. 5 and vary α . The four (α,σ) -points (triangles) along this segment correspond to the parameters used to find the orbits seen in Fig. 6, which are pictured using triangles of the same color. Figure 6 also shows the heteroclinic orbit that lies on the 1D unstable manifold of the fixed point ξ_- (black triangle) to the attracting orbit. This unstable manifold is traced out by 500 iterates of a set of 100 initial conditions starting in a ball of radius 0.01 about ξ_- . The first point, at $\alpha \approx -0.248$, is a stable period-one orbit. It period doubles at $\alpha \approx -0.393$, creating an attracting period-2 orbit, shown for $\alpha \approx -0.563$ (orange triangles). The 1D unstable manifold of ξ_- is also shown in orange. As α continues to decrease, the doubling

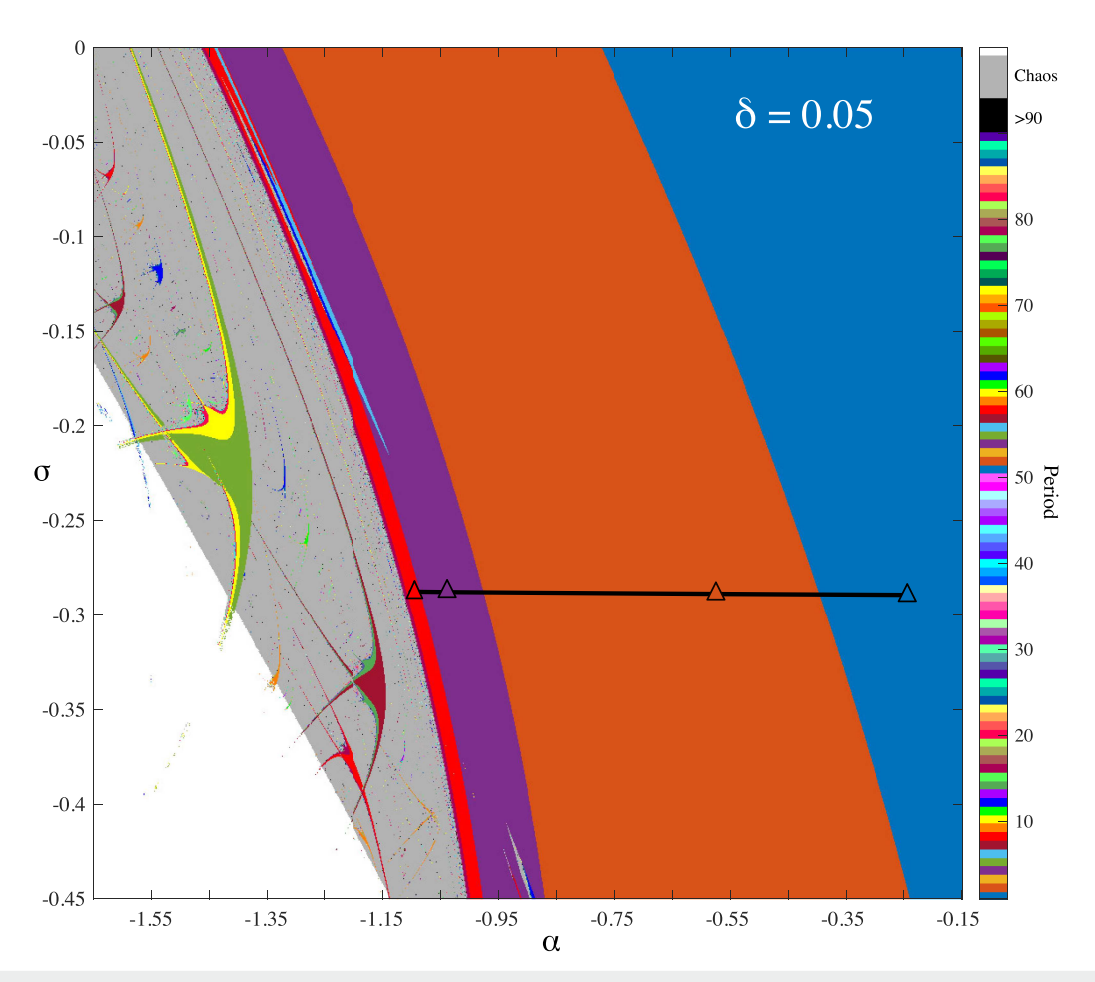


FIG. 5. An enlargement of case (SC) from Fig. 4(a), providing more detail of the period-doubling cascade. The triangles along the line segment show parameters used in Fig. 6. Also seen are a number of *shrimps* corresponding to period-5 (dark green), period-7 (brown), etc., attracting orbits.

recurs forming next a stable period-4 (magenta) and then a stable period-8 (red). The parameters for these are listed in Table II.

Also prominent in Fig. 5 are a number of *shrimps*, common structures seen in two-parameter families of one^{27,28} and two-dimensional maps.²⁹ Shrimps are prototypical structures formed by saddle-node bifurcations of periodic orbits in a "sea of chaos." These structures will not be discussed further in this paper.

B. Resonant tongues

At a resonant point, $\omega = \frac{p}{q}$, on the NS curve, a pair of period-q orbits are born when $q \ge 5$. These period-q orbits exist in a "tongue"-shaped region bounded by curves of SN bifurcations. While a pair of periodic orbits still exist for the strongly resonant cases, $q \le 4$, the resonant regions can be more complex.³ Near the NS curve of the fixed point, one of these orbits is stable and is easily detected by our recurrence algorithm. Such tongues are especially prominent in Fig. 7 for case (MC).

The pair of orbits found within the tongues can be used to find heteroclinic orbits from the period-q saddle to its attracting counterpart. Examples for q=3 and 4 are seen for case (MC) in Fig. 8. The parameters chosen in the respective tongues are indicated in Fig. 7 by triangles and listed in Table II. To visualize the heteroclinic orbits, a set of 100 initial conditions are chosen in a ball of radius 0.01 about a point on the period-q saddle, which is found by numerically solving for a fixed point of $L^q(\xi)$. The first 500 iterates of these points, shown in Fig. 8, trace out the 1D unstable manifold of the saddle and lie on the 2D stable manifold of the period-q sink.

VI. APERIODIC ATTRACTORS

We now discuss the black and gray regions seen in Fig. 4 and its enlargements (Figs. 5 and 7). These represent parameters for which there is an attractor that is either aperiodic or periodic with the period larger than 90. Possible aperiodic attractors include invariant circles formed at an NS bifurcation with irrational ω , as

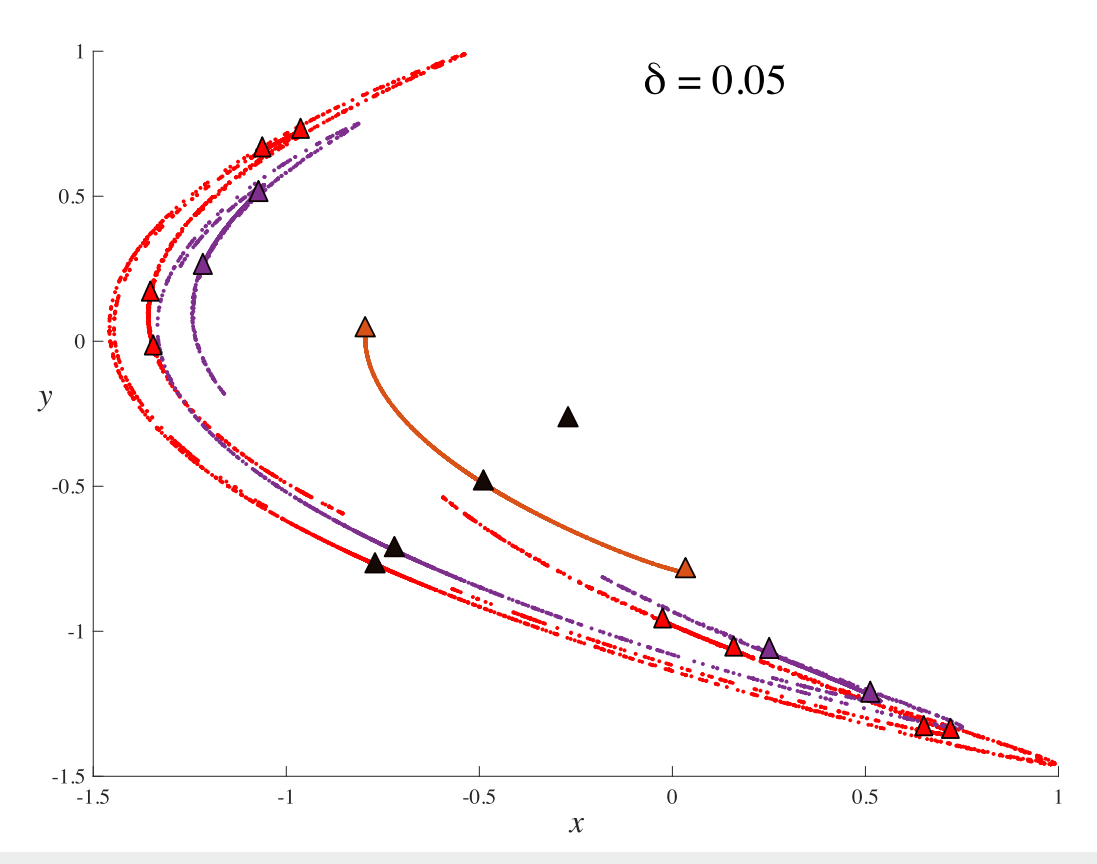


FIG. 6. Four orbits along the period-doubling cascade for case (SC) for parameters given in Table II. For each, the fixed point is shown as a black triangle and attracting orbits as triangles colored by period using the same color scheme as Fig. 5. At first, there is a single fixed point, and as α decreases, the fixed point shifts down and leftward, becoming a reflecting saddle when it bifurcates creating a period-2 attractor (orange). This process repeats for period-4 (magenta) and period-8 (red). A heteroclinic orbit of the same color connects the fixed point and attracting orbit.

well as more complex, possibly chaotic cases. In this section, we will distinguish between regular and chaotic cases by computing the maximal Lyapunov exponent. In a number of studies, multiple Lyapunov exponents were calculated to characterize the dimensionality of the unstable spaces of attractors. ^{16,22} Here, we only compute one, as our focus is simply the distinction between chaotic and regular.

Formally, the Lyapunov exponent is

$$\mu(\xi_0; \nu_0) = \limsup_{n \to \infty} \frac{\ln \|\nu_n\|}{n}$$
 (18)

for an initial point ξ_0 and an initial vector v_0 , which evolves linearly as $v_t = DL(\xi_{t-1})v_{t-1}$. Note for a generic initial vector, v_0 , this limits to the maximal exponent (MLE). If there exists an attracting regular

TABLE II. Parameters for Figs. 6 and 8 that correspond to the annotations in Figs. 5 and 7.

Case	Behavior	$(lpha,\sigma)$	△ Color
$\delta = 0.05$	Fixed point	(-0.24830, -0.29130)	Black
	Doubling bifurcation	(-0.39312, -0.29130)	
	Period-2 attractor	(-0.56271, -0.29130)	Orange
	Quadrupling bifurcation	(-0.97316, -0.29130)	_
	Period-4 attractor	(-0.99417, -0.29130)	Magenta
	Octupling bifurcation	(-1.08197, -0.29130)	_
	Period-8 attractor	(-1.09922, -0.29130)	Red
$\delta = 0.7$	Period-3 attractor	(-0.13557, 0.28892)	Yellow
	Period-4 attractor	(0.105 53, 1.009 50)	Magenta

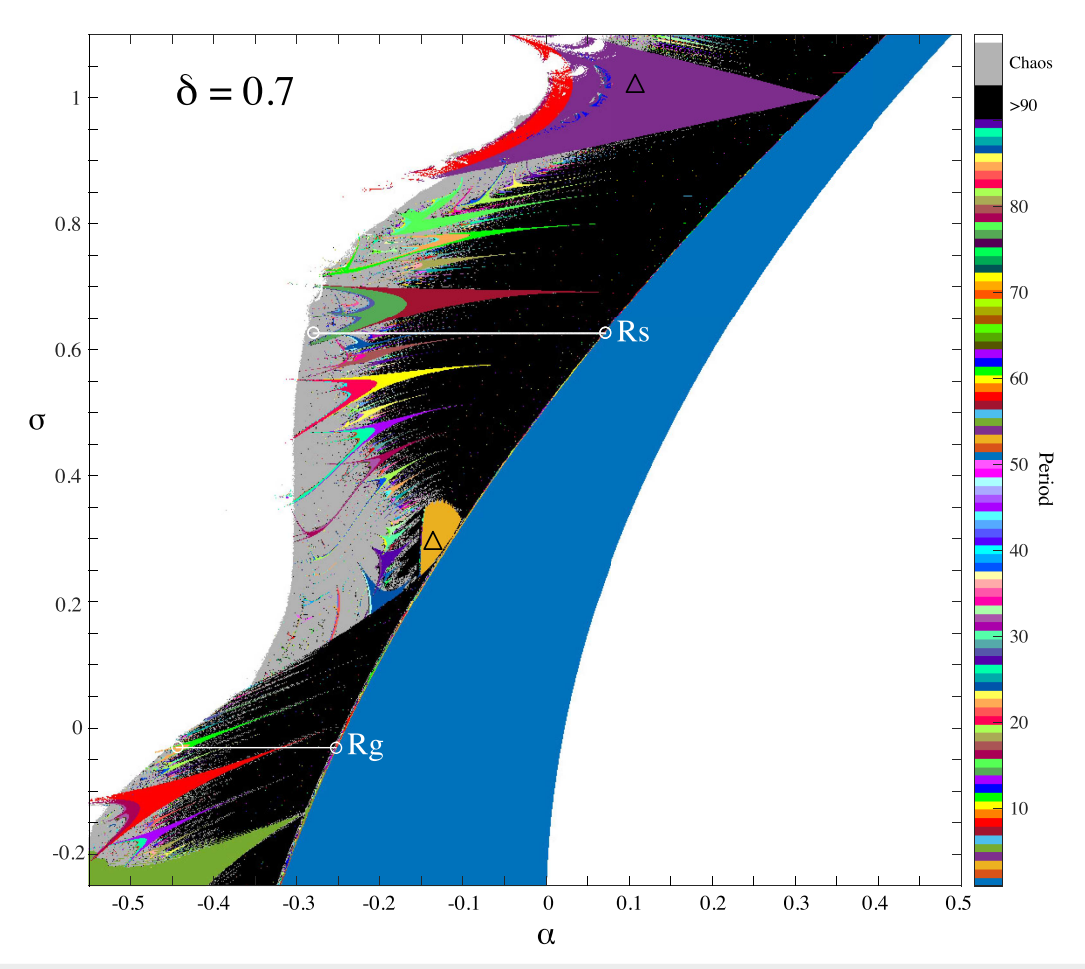


FIG. 7. An enlargement of case (MC) from Fig. 4(b) provides detail of the resonant tongues emanating from the NS line of ξ_- . Highlighted points include two triangles in the period-3 and 4 tongues, used for the phase portraits in Fig. 8. Also shown are line segments Rg and Rs that have endpoints along the NS line that correspond to $\omega = 2/(1 + \sqrt{5})$, the golden mean, and $\omega = 1/\sqrt{2}$, the silver mean. The behavior of orbits in phase space along these segments are discussed in Sec. VI A.

orbit, then any initial condition in its basin will have a non-positive MLE, whereas chaotic orbits will have $\mu>0$.

Numerically, we approximate the lim sup of (18) by choosing an increment ΔT and computing

$$\mu_T(\xi_0; \nu_0) = \max_{n \in [T, T + \Delta T)} \frac{\ln \|\nu_n\|}{n}.$$
 (19)

This approximates (18) for a "large" enough T and ΔT , up to some tolerance. We estimate the MLEs for those bounded orbits that have periods larger than 90. The initial point used for (19) is the point used in the recurrence algorithm described in Sec. V found after 5000 + 90 iterates, and the initial vector is set to $v_0 = (1, 1, 1)/\sqrt{3}$. To avoid overflow, the length of v_n is renormalized every ten iterates. As is well known, it is computationally expensive to achieve convergence of MLEs. Indeed, since the ostensible error for (19) is $\mathcal{O}(T^{-1})$, we chose a threshold appropriate for $T \sim 10^3 - 10^4$: an

orbit is deemed regular if $\mu_T \leq \mu_o = 3(10)^{-4}$. We selected the interval $\Delta T = 100$ as it gave reasonable convergence for a number of trials. The time T in (19) is increased in steps of ΔT until the error $|\mu_T - \mu_{T+\Delta T}| < 10^{-4}$ or until T reaches $T_{\rm max} = 10^5$. In this case, the MLE is set to $\mu_{T_{\rm max}}$. For the results in Fig. 4, μ_T is set to $\mu_{T_{\rm max}}$ for 0.14% of the calculations for case (MC) and 1.2% for case (SC).

Orbits with $\mu_T > \mu_o$ are declared to be "chaotic" and colored gray, and those with smaller MLEs are declared "regular" and colored black in the figures. As seen in Fig. 4. there is a qualitative difference between the two cases. For case (SC), there are very few regular, aperiodic orbits—these are confined to a narrow strip along the NS curve at the top of the bounded region (4.3% of the aperiodic orbits). For case (MC), however, there are large regions of regular, aperiodic behavior to the left of the NS curve (70% of the aperiodic orbits). In Subsections VI A and VI B, we illustrate this difference by looking at the corresponding behavior of orbits in phase space.

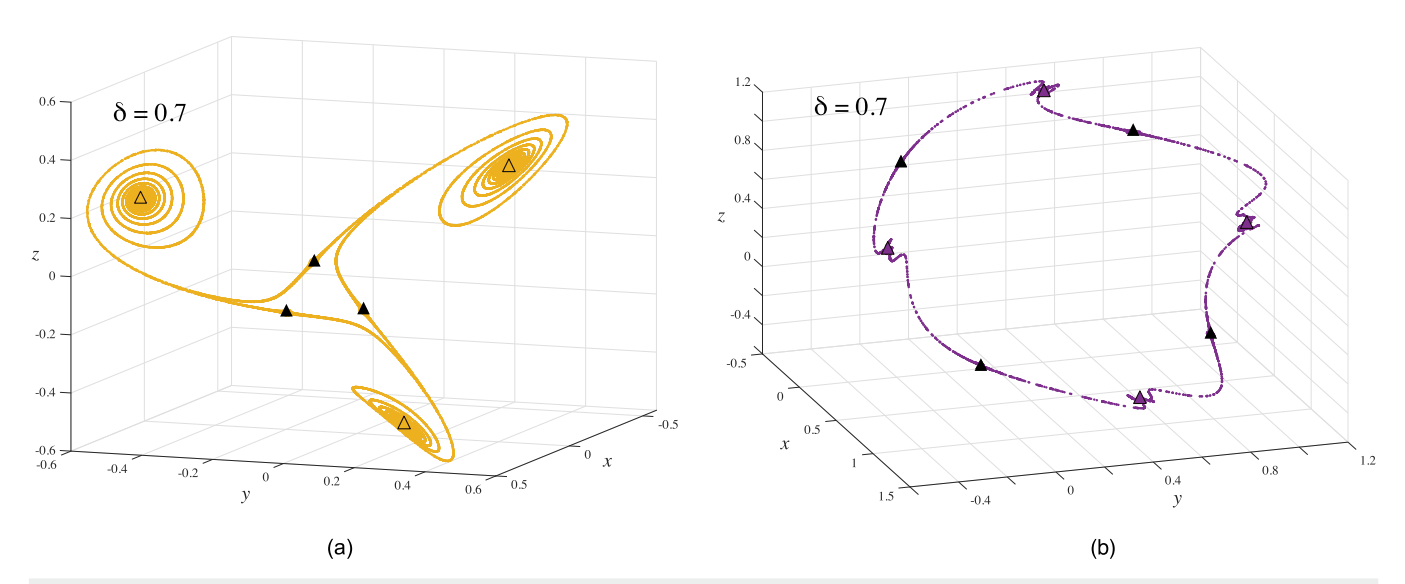


FIG. 8. Two heteroclinic orbits for the (MC) case found in the period-3 (yellow, left) and 4 (magenta, right) tongues, respectively. These orbits connect the periodic saddle orbit (black triangles) with its attracting periodic counterpart (yellow and magenta triangles). See Table II for values of (α, σ) .

A. Regular attractors

Regular, aperiodic orbits are primarily born on the NS curve when the rotation number, ω , in (6) is irrational. Such a bifurcation generically gives rise to an invariant circle that persists for an interval along a curve in parameter space that starts on the NS curve. The rotation number will become rational when the curve enters a resonant tongue. To explore the structure of such circles, we study the development of orbits in phase space for (MC) along two lines in the (α, σ) -plane that start at an irrational NS point, as illustrated in Fig. 7.

Rg:
$$\sigma_g \approx -0.03232$$
, $(\alpha_{g0}, \alpha_{g1}) \approx (-0.25375, -0.45269)$, (20)

Rs:
$$\sigma_s \approx 0.62724$$
, $(\alpha_{s0}, \alpha_{s1}) \approx (0.07064, -0.28960)$. (21)

The Rg segment starts at (α_{g0},σ_g) , the NS bifurcation for the golden mean, $\omega=\frac{1}{2}(\sqrt{5}-1)\approx 0.618\,03$, and the Rs segment starts at (α_{s0},σ_s) , the NS bifurcation for the silver mean, $\omega=\frac{1}{\sqrt{2}}\approx 0.707\,11$. Each segment has fixed σ and ends when α reaches the edge of the bounded region.

Figure 9 shows orbits along (20), starting just below α_{g0} and moving toward α_{g1} in six panels. These are projected onto the plane orthogonal to the line x = y = z that contains the fixed points. This plane is spanned by the orthogonal vectors

$$u = (-1, 1, 0), \quad v = (1, 1, -2),$$
 (22)

and these are used as the axes in the figures. We observe that the invariant circles appear to have a one-to-one projection onto this plane and enclose the projected fixed point ξ_- , which projects to the origin (black triangle). Each panel consists of several orbits; corresponding values of α are given. As α decreases, an invariant circle

grows, deforms, and bifurcates to periodic orbits when the segment passes through resonant tongues.

An alternative visualization of the dynamics along (20) is through its bifurcation diagram, seen in Fig. 10 (top, left). This shows a 1D projection onto the x-axis for varying α . Invariant circles correspond to dense segments and periodic attractors to isolated points in this diagram.

Following the analysis of Ref. 12, we compute the rotation number of the orbits. Since the projection onto the (u, v) plane is one-to-one and encircles the origin, the rotation number can be computed by measuring the angle θ_t at time t counterclockwise from the vector u using the full range atan2 function. The time T approximation of the rotation number is then

$$\omega_T = \frac{1}{2\pi T} \sum_{t=1}^T \theta_t. \tag{23}$$

This sum is computed from the initial conditions used for Fig. 7 after removing the transient as before. We choose T to be the return time (17) or if there is no such time, $T = 5(10)^5$. For the purposes of our illustrations, this gives sufficient accuracy. If one desired higher accuracy computations, then the sum in (23) could be replaced by a weighted average as discussed in Ref. 30.

The rotation number and the corresponding Lyapunov exponent, (19), are shown as a function of α in the bottom row of Fig. 10, aligned with the corresponding bifurcation diagrams for (20) and (21).

We do not observe chaotic orbits along (20)— μ_T is essentially nonpositive, though small oscillations up to the threshold μ_o reflect the difficulty in computing the MLE. Note that when the dynamics are conjugate to a rigid rotation (i.e., the orbit lies on a circle), then there is a zero Lyapunov exponent. Since the circle is attracting, this is what we observe for the MLE in Fig. 7. When $\alpha \approx \alpha_{\rm g0}$, the rotation

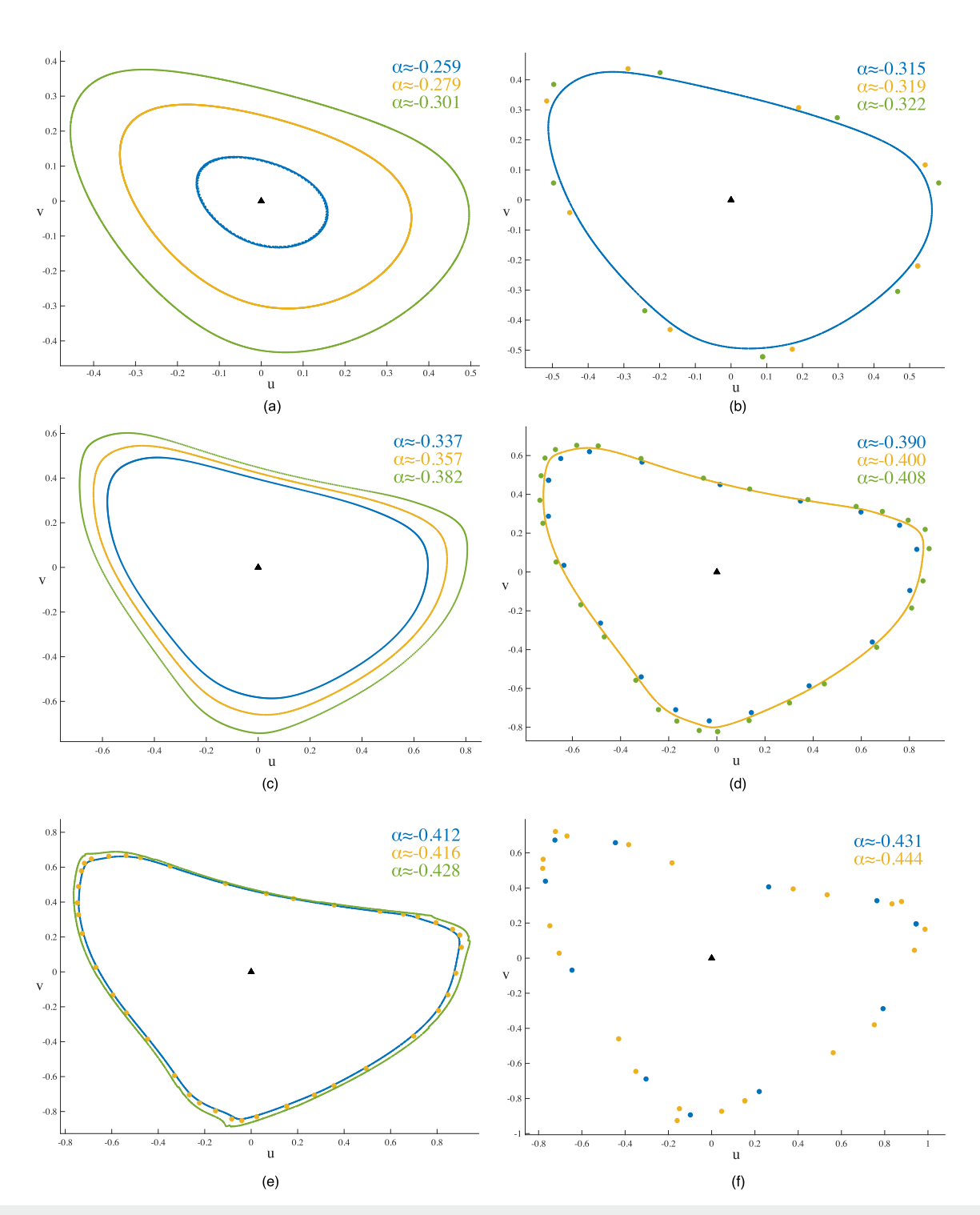


FIG. 9. Attracting orbits found along (20), seen in Fig. 7, projected onto the plane (22). The black triangle at the origin is the projected fixed point, ξ_- . Each panel contains two or three orbits for values of α shown in the same color as the orbit. The panels correspond to the intervals at the bottom of Fig. 10 (left). (a) Invariant circles close to α_{g0} . (b) An invariant circle and two period-8 orbits. (c) Three invariant circles. (d) Period-19 (blue) and period-30 (green) orbits, with an invariant circle at an intermediate α . These periodic orbits lie in windows too small to be visible in Fig. 10 (left). (e) Two invariant circles and a period-41 orbit at an intermediate α . (f) Period-11 (blue) and doubled period-22 (yellow) orbits. All of these orbits are regular, as $\mu_T < \mu_o$ along the entire segment, seen in Fig. 10 (left). Orbits become divergent when $\alpha \le \alpha_{g1}$.

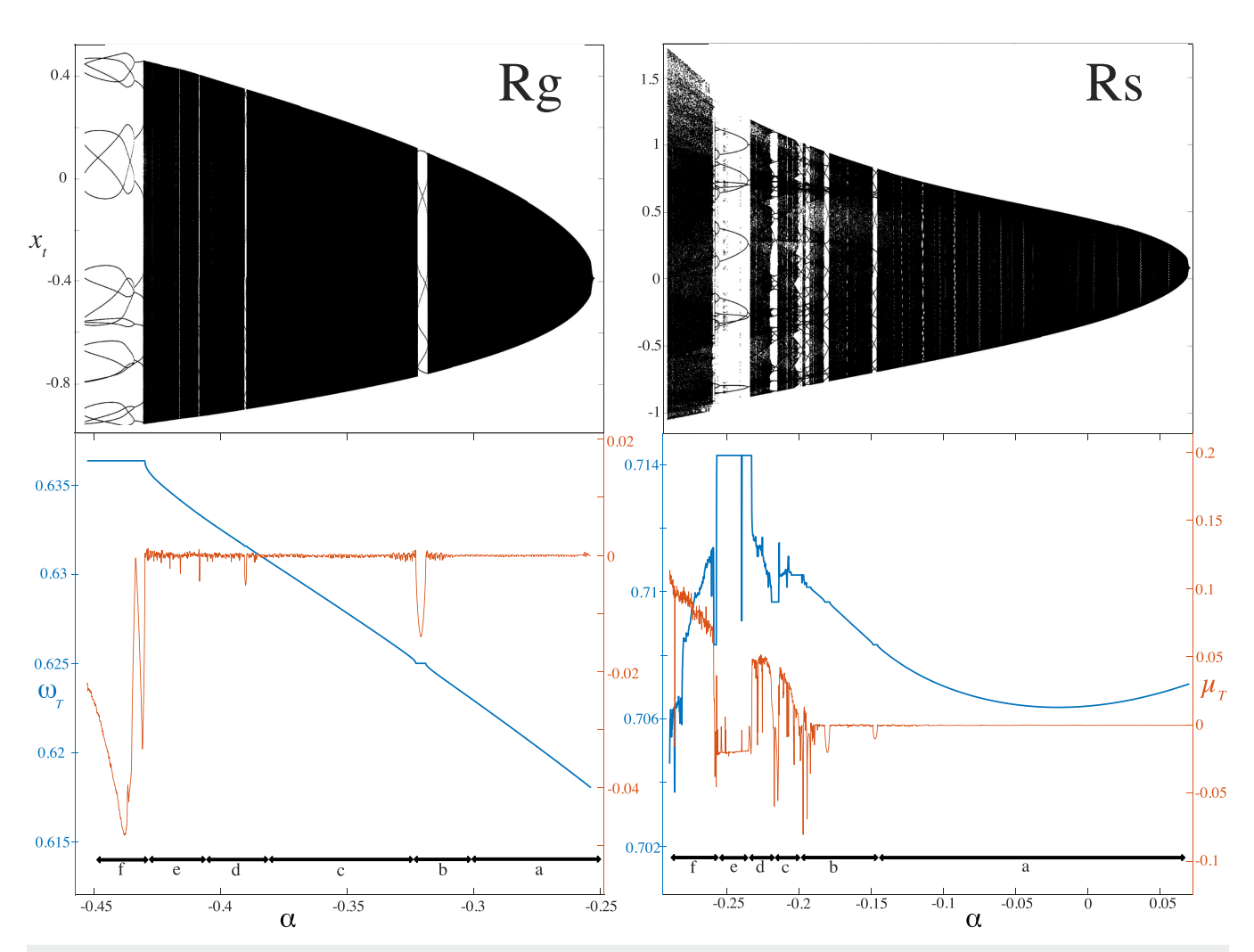


FIG. 10. Bifurcation diagrams (top) aligned with graphs of ω_T and μ_T (bottom) for attracting orbits along the segments (20) (left) and (21) (right). Calculations start with an α value 10^{-4} below the NS points, and α is decreased until the orbits diverge (i.e., when the segment reaches the white region). Resonant tongues correspond to constant ω_T in the bottom panels and to windows of periodicity in the top panels. Chaotic orbits, $\mu_T > \mu_o$, are only seen for (21). The annotated α intervals, (a)–(f), refer to the panels of Figs. 9 and 11.

number $\omega_T \approx 0.618$, as expected, and as α decreases, the rotation number grows monotonically. When the orbit passes through a resonant tongue, ω_T becomes a constant rational value and $\mu_T < \mu_0$ since the resulting periodic orbit is attracting. These align with the periodic windows in the bifurcation diagram. Periodic windows visible in Fig. 10 (left) are the period eight ($\omega = \frac{5}{8} = 0.625$) and the period 11 and 22 tongues. For the latter, $\omega = \frac{7}{11} \approx 0.636$, and—when the orbit doubles— $\omega = \frac{14}{22}$, the same value. Near the period doubling in the $\frac{7}{11}$ tongue, μ_T grows as α decreases, reaching zero at the bifurcation point $\alpha \approx -0.433$. The orbit diverges when $\alpha \leq \alpha_{\rm g1}$.

The segment (21) crosses multiple tongues and chaotic regions, as seen in Fig. 10 (right). When $\alpha \approx \alpha_{s0}$, $\omega_T \approx 0.707$, but as α decreases, the rotation number is not monotone. Note that when

 $\mu_T > \mu_o$, calculations for ω_T do not converge well since the orbit is chaotic. As before, in the resonant tongues, $\mu_T < \mu_o$ and ω_T is constant, and when there is an attracting invariant circle, μ_T is close to zero. The most visible tongues correspond to orbits of period 24 ($\omega = \frac{17}{24} \approx 0.708$), 31 and 62 ($\omega = \frac{22}{31} = \frac{44}{62} \approx 0.710$), and 7 and 14 ($\omega = \frac{5}{7} = \frac{10}{14} \approx 0.714$). Note that there are chaotic regions both before and after the last tongue.

Phase portraits along (21) projected onto the plane (22) are shown in a series of six panels in Fig. 11; each corresponds to an interval annotated in Fig. 10 (right). Near α_{s0} , we observe a family of growing invariant circles that pass through windows of periodicity as α decreases. Panels (c), (d), and (f) show chaotic attractors; these occur when the segment (21) passes through gray regions so that $\mu_T > \mu_o$, in Fig. 10 (right). These attractors are born with a structure

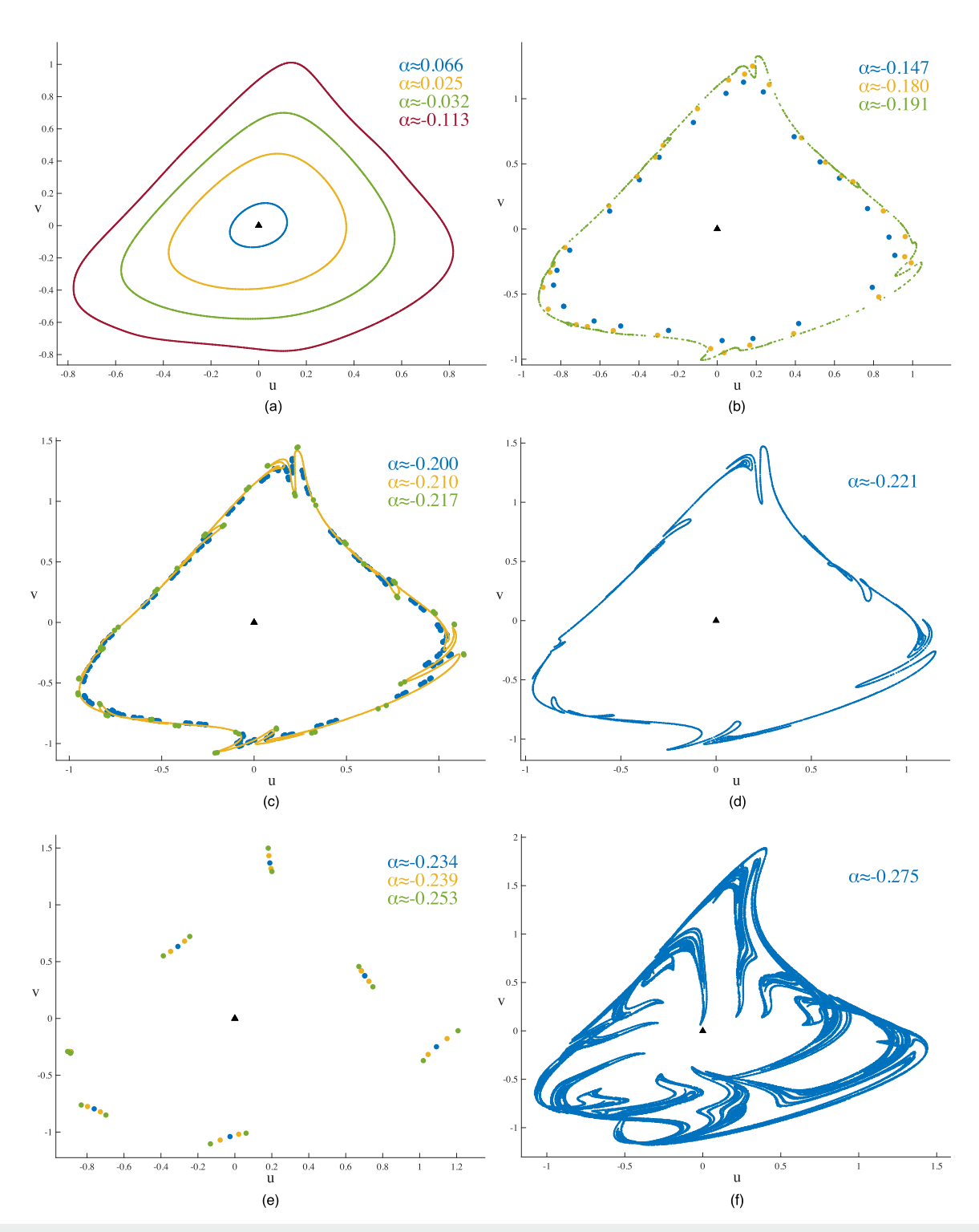


FIG. 11. Attracting orbits along (21), a segment in Fig. 7, projected onto the plane (22). The black triangles are the fixed point, ξ_- . Each panel contains orbits at the indicated values of α in the same color as the orbit. The panels correspond to the intervals labeled in Fig. 10 (right). (a) Four invariant circles near α_{s0} . (b) Period-24 (blue), period-31 (yellow), and an invariant circle. (c) Period-608 (blue), chaotic with $\mu_T=0.14771$ (yellow), and period-62 (green) orbits. (d) Chaotic orbit with $\mu_T=0.23646$. (e) Period-7 orbit (blue) that doubles to period-14 (yellow and green). (f) Chaotic orbit with $\mu_T=0.48808$. This attractor is shown in 3D in Fig. 13(a). Orbits become divergent for $\alpha \leq \alpha_{s1}$.

like the invariant circle but also seem to fold around the neighboring, no-longer stable periodic orbits. In panel (f), the outer boundary of the chaotic attractor appears relatively smooth and aligns with the former invariant circle, but its interior is much more complex. This attractor is also shown in 3D in Fig. 13(a).

B. Chaotic attractors

As we have known since Feigenbaum's classic studies of 1D maps, chaos can arise from a self-similar accumulation of period-doubling bifurcations, i.e., a period-doubling cascade.^{2,3} As we have seen for (1), cascades from the fixed point ξ_- , Fig. 5, or from higher period orbits, at the "ends" of the tongues, Fig. 7, do indeed lead to chaos

When δ is small, the resulting chaotic attractors can resemble that of the 2D Hénon map. For case (SC), where $\delta=0.05$, the heteroclinic orbits of Fig. 6 show the beginning of the development of a Hénon-like attractor through a period-doubling cascade of the fixed point. Continuing beyond the end point of the segment in Fig. 5 leads to the attractor shown in Fig. 12(a), with a nearly 2D, horseshoe-like shape. Note that for $\delta=0$, the map (1) is essentially 2D (it becomes a semi-direct product of a linear map and a 2D quadratic map 14), and for $(a,c,\alpha,\sigma)=(1,0,-1.4,-0.3)$, its dynamics correspond to the classic Hénon map. Even when $\delta=0.05$, these parameters are at the very edge of the chaotic region after the period-doubling cascade of the fixed point, close to an arm of the period-5 shrimp in Fig. 5. The attractor for this case is shown in Fig. 12(b).

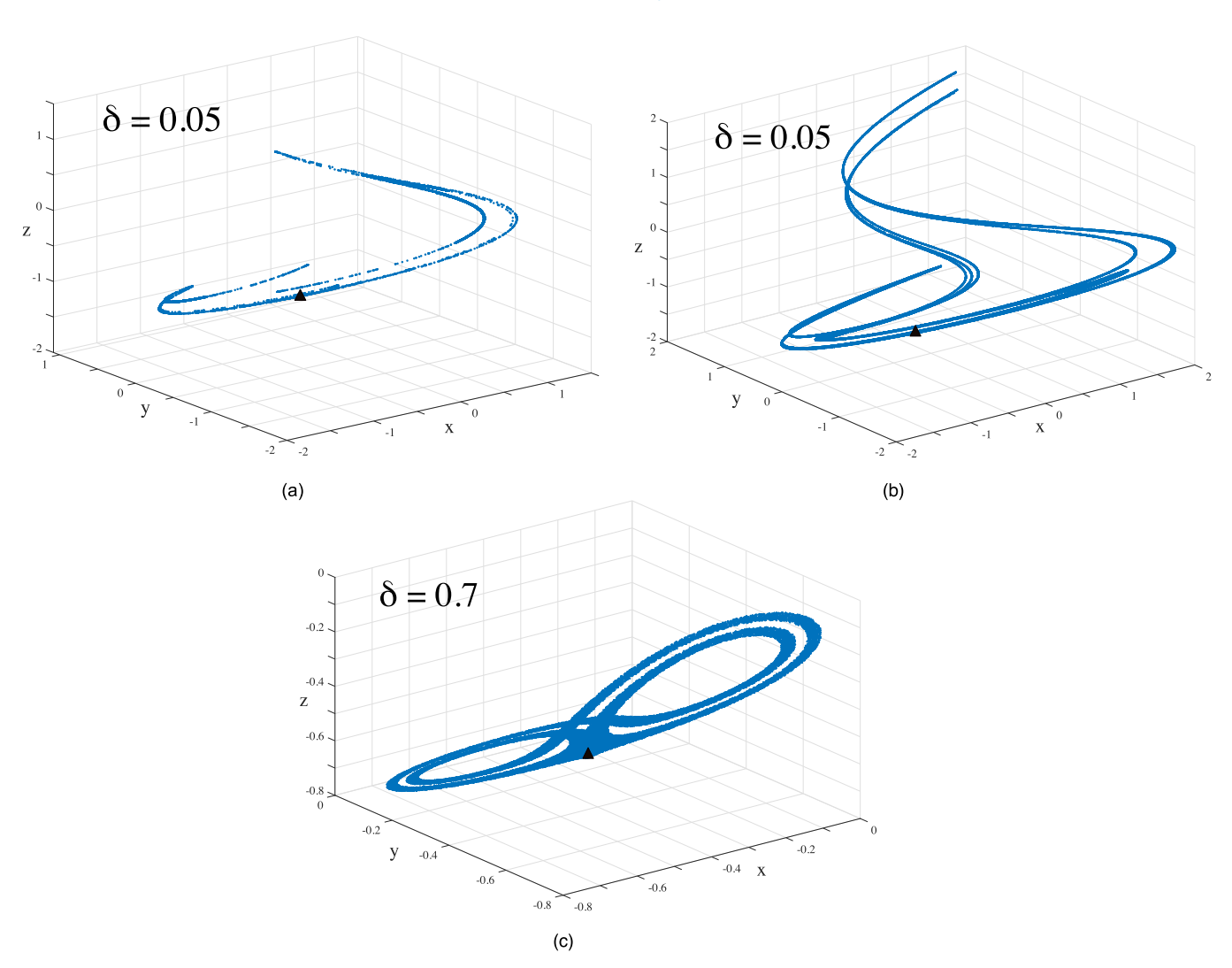


FIG. 12. Chaotic attractors illustrated as 500 iterates of 100 points in a ball of radius 0.01 about the fixed point ξ_- (black triangle). (a) Case (SC) with $(\alpha, \sigma) \approx (-1.135\,99, -0.291\,30)$ following from the heteroclinic orbit seen in Fig. 6 after a period-doubling cascade. (b) Case (SC) with $(\alpha, \sigma) = (-1.4, -0.3)$, near the parameters of the classic Hénon attractor. (c) A Lorenz-like attractor for case (MC) with $(\alpha, \sigma) = (0, -0.815)$.

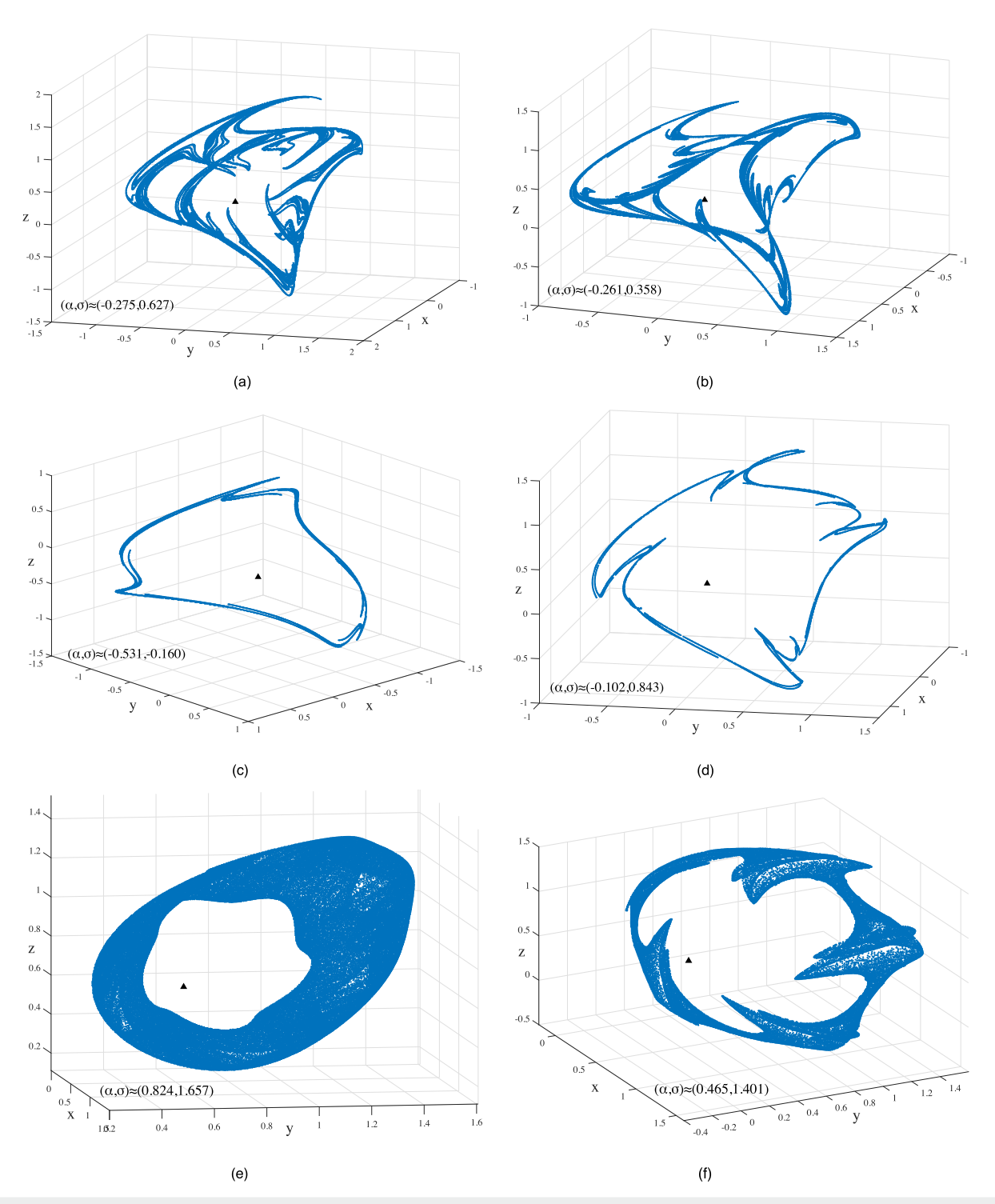


FIG. 13. Chaotic attractors found using the method described in Sec. VI A: a point near ξ_- (black triangle) is first iterated 5000 steps to remove transients, and then T additional points [T is either the return time (17) or at most $5(10)^5$] are plotted. (a) A 3D view of the attractor of Fig. 11(f) for case (MC). (b)–(f) Attractors for case (MC) for five parameter cases (shown in each panel) taken from the chaotic (gray) regions of Fig. 4(b).

In Ref. 22, parameters were found so that a 3D quadratic map conjugate to (1) has a discrete Lorenz-like attractor. The corresponding parameters for (1) are $(a, c, \delta, \alpha, \sigma) = (1, 0, 0.7, 0, -0.815)$. This case lies within the chaotic region below the NS bifurcation of the period-two orbit shown in Fig. 4(b). The resulting Lorenz-like attractor (with a lacuna) is shown in Fig. 12(c). We refer to the works of Gonchenko *et al.* 16,22 for more discussions of such attractors.

In Sec. VI A, we saw the development of chaotic attractors as α decreased along the segment (21); recall Figs. 11(c), 11(d), and 11(f). A three-dimensional plot of panel (f) is shown in Fig. 13(a) to better illustrate that it appears to lie near a paraboloid that opens up in the positive direction along the line x=y=z, which is near the local unstable manifold of the fixed point ξ_- . To illustrate some of the variations in geometry that can occur, five additional cases, using parameters in the gray region of Fig. 4(b) for case (MC), are also pictured in Fig. 13. As before, each of these appears to lie near a paraboloid. The attractors in panels (a) and (b) have arms or tentacles, some of which appear to go toward the fixed point ξ_- . By contrast, in panels (b) and (c), the attractors more closely resemble invariant circles with additional folds. Finally, in panels (e) and (f), the attractors have an internal flower-like structure that fills out an annular region on the paraboloid.

VII. CONCLUSIONS

Previous research on quadratic 3D maps has focused on the volume-preserving case^{8,12} or on the existence and development of chaotic attractors.^{4,16,22} Here, we have explored a broader range of parameters and studied periodic and aperiodic, and regular and chaotic attractors.

The simplest bifurcations of a 3D map were discussed in Sec. II using the trace and second trace of the Jacobian as primary parameters and fixing the Jacobian determinant. These results were applied to the fixed points of the map (1) in Sec. III. We focused on two primary parameters: the more "structural" parameter σ , which controls the *type* of bifurcation and what can be viewed as the "primary unfolding" parameter, α . Note that in our previous work on antiintegrability, it was the limit $\alpha \to -\infty$ that corresponded to a non-deterministic limit where the dynamics is conjugate to a shift on a set of symbols. ¹⁴

For our numerical studies, we chose two cases for the Jacobian δ : a strongly contracting case (SC)—where the map is nearly 2D—and a moderately contracting case (MC).

We showed in Sec. IV that all bounded orbits of the orientation preserving 3D Hénon map lie within a cube about origin as illustrated in Fig. 3. Most of the region of bounded orbits corresponds to nonchaotic situations, which could be an attracting fixed point or orbits that arise from this point by doubling or Neimark–Sacker bifurcations. However, this figure also shows protruding spikes from the region of stability, which may be related to attractors not born from the fixed point. We hope to study these further in the future.

To classify the behavior of bounded orbits, we computed resonant regions in parameter space in Sec. V; these are analogous to the Arnold tongues of circle maps. The resulting partition of the bounded region, Fig. 4, shows periodic and aperiodic attractors. Using this, we are able to understand the development of attracting periodic orbits and visualize their codimension-one and -two

bifurcations. Note that our computations used the attractor arising from a single initial condition. There will be cases with multiple attractors and cases for which the chosen orbit is unbounded even when there might be attractors elsewhere. However, given the similarity between Figs. 3 and 4, the latter possibility is rare. We plan to investigate the more complex, outlying cases in future research.

Aperiodic attractors (defined to be attractors with period greater than 90) were studied in Sec. VI. We also followed the evolution of invariant circles along several curves in parameter space starting at points on the NS bifurcation curve where the rotation number was irrational. We did not attempt to follow a circle with fixed rotation number, though we expect such a curve exists in a two-dimensional parameter space and plan to do this in future research. Along the parameter curves that we did follow, the invariant circle has a varying rotation number. When this becomes rational, the circle undergoes a resonant bifurcation, generically breaking up into a pair of periodic orbits. Given the hyperbolic structure of these attractors, this could lead to a "string of pearls" bifurcation as discussed in Ref. 12, which results in the formation of bubbles from the stable and unstable manifolds of the periodic orbits. Such bifurcations were also seen for a normal form near a codimensiontwo SN-NS bifurcation in Ref. 31. These cases will be analyzed in future work. As the curve leaves a resonant tongue, an invariant circle can reform. In some cases, the destruction of the circle gave rise to chaotic attractors.

Some of the chaotic attractors we studied are well known: the discrete Lorenz and Hénon attractors found in Refs. 1, 14, and 22. More unusual are the chaotic attractors with a paraboloid structure that arise from the destruction of the invariant circles; recall Fig. 13. These are not classified in Ref. 16 and are not obviously related to the 3D generalized horseshoes studied by Ref. 25. We believe that further study of such cases could lead to a broader understanding of attractors that lie within higher-dimensional generalizations of the Smale horseshoe.

ACKNOWLEDGMENTS

The authors acknowledge support from the National Science Foundation grant (No. DMS-1812481).

AUTHOR DECLARATIONS

Conflict of Interest

The authors have no conflicts to disclose.

Author Contributions

Amanda E. Hampton: Conceptualization (equal); Data curation (equal); Formal analysis (equal); Investigation (equal); Methodology (equal); Validation (equal); Visualization (equal); Writing – original draft (equal); Writing – review & editing (equal). James D. Meiss: Conceptualization (equal); Data curation (equal); Formal analysis (equal); Funding acquisition (equal); Investigation (equal); Methodology (equal); Project administration (equal); Supervision (equal); Validation (equal); Visualization (equal); Writing – original draft (equal); Writing – review & editing (equal).

DATA AVAILABILITY

The data that support the findings of this study are available within the article.

APPENDIX: PARAMETER SPACE CONVERSION

Here, the conditions for codimension-one and -two bifurcations as seen in the last column of Table I in terms of the trace and second trace are converted to conditions on (α, σ) . We are interested in the fixed point ξ_- of (1), given by (8); thus, t and t are given by (10) and t and t as sume that t and t are given by (10) and t and t as sume that t and t are given by (10) and t and t as sume that t and t are given by (10) and t and t are given by (10) and t and t are given by (10) and t ar

Provided that there are no singularities, the codimension-one bifurcation curves are easily found using (9),

(SN)
$$\alpha = \frac{1}{4}(\sigma - \delta + 1)^2$$
,
(PD) $\alpha = x_{PD}(2x_{SN} - x_{PD})$, (A1)
(NS) $\alpha = x_{NS}(2x_{SN} - x_{NS})$

for $x_{SN} = \frac{1}{2}(\sigma - \delta + 1)$ and x_{PD} , x_{NS} given by (12) and (13), respectively. The NS bifurcation is restricted to the interval $\delta - 2 < (2a + b)x_{NS} < \delta + 2$.

Again, provided there are no singularities, the codimensiontwo bifurcations are all points that satisfy (9) but also require an expression for σ . The SNf bifurcation occurs at $(t,s)=(-\delta,-1)$. Using t to solve for the fixed point then gives

(SNf)
$$x_{SNf} = -\frac{\delta}{2a+b},$$

$$\alpha = x_{SNf}(2x_{SN} - x_{SNf}),$$

$$\sigma = -1 + (b+2c)x_{SNf},$$

where x_{SN} is dependent on σ .

A Neimark–Sacker bifurcation with rotation number ω occurs at $(t,s)=(2\cos{(2\pi\omega)}+\delta,\delta(t-\delta)+1)$. Solving for the fixed point then gives

(R
$$\omega$$
)
$$x_{R\omega} = \frac{2\cos(2\pi\omega) + \delta}{2a + b},$$
$$\alpha = x_{R\omega}(2x_{SN} - x_{R\omega}),$$
$$\sigma = 2\delta\cos(2\pi\omega) + 1 + (b + 2c)x_{R\omega},$$

where, again, x_{SN} is dependent on σ .

Last, recall that double multipliers, $\lambda_{1,2} = r \in \mathbb{R}$, occur on the parametric curves (7). Using the same process as above yields

$$(\lambda_1 = \lambda_2)$$

$$x_r = \frac{\delta + 2r^3}{r^2(2a+b)},$$

$$\alpha = x_r(2x_{SN} - x_r),$$

$$\sigma = 2\frac{\delta}{r} + r^2 + (b+2c)x_r$$

for x_{SN} dependent on σ . Since we are only concerned with x_- and we know $x_- < x_{SN}$, we choose r such that $x_r < x_{SN}$. When enforcing (2), we obtain the range $|r| > \sqrt{\delta}$; otherwise, $x_r = x_+$.

REFERENCES

¹M. Hénon, "A two-dimensional mapping with a strange attractor," Commun. Math. Phys. **50**, 69–77 (1976).

²J. Guckenheimer and P. Holmes, *Nonlinear Oscillations, Dynamical Systems, and Bifurcations of Vector Fields*, Applied Mathematical Sciences Vol. 42 (Springer-Verlag, New York, 2002).

³Y. Kuznetsov, *Elements of Bifurcation Theory*, 3rd ed., Applied Mathematical Sciences Vol. 112 (Springer-Verlag, New York, 2004).

⁴S. Gonchenko, I. I. Ovsyannikov, C. Simó, and D. Turaev, "Three-dimensional Hénon-like maps and wild Lorenz-like attractors," Int. J. Bifurcation Chaos 15, 3493–3508 (2005).

⁵R. Devaney and Z. Nitecki, "Shift automorphisms in the Hénon mapping," Commun. Math. Phys. **67**, 137–146 (1979).

⁶M. Benedicks and L. Carleson, "The dynamics of the Hénon map," Ann. Math. 133, 73–169 (1991).

⁷D. Sterling and J. Meiss, "Computing periodic orbits using the anti-integrable limit," Phys. Lett. A **241**, 46–52 (1998).

⁸H. Lomelí and J. Meiss, "Quadratic volume-preserving maps," Nonlinearity 11, 557–574 (1998).

PZ. Elhadj and J. Sprott, "Classification of three-dimensional quadratic diffeomor-

phisms with constant Jacobian," Front. Phys. Chin. 4, 111–121 (2009).

10 K. Lenz, H. Lomelí, and J. Meiss, "Quadratic volume preserving maps: An

extension of a result of Moser," Regul. Chaotic Dyn. 3, 122–130 (1999).

11 H. Dullin and J. Meiss, "Nilpotent normal forms for a divergence-free vector

fields and volume-preserving maps," Physica D 237, 155–166 (2008). $^{12}\rm H.$ Dullin and J. Meiss, "Quadratic volume-preserving maps: Invariant circles

and bifurcations," SIAM J. Appl. Dyn. Syst. 8, 76–128 (2009).

18 S. V. Gonchenko, J. Meiss, and I. Ovsyannikov, "Chaotic dynamics of three-dimensional Hénon maps that originate from a homoclinic bifurcation," Regul.

Chaotic Dyn. 11, 191–212 (2006).

14A. Hampton and J. Meiss, "Anti-integrability for three-dimensional quadratic

maps," SIAM J. Appl. Dyn. Syst. **21**, 650–675 (2022).

15 D. Turaev and L. Shilnikov, "An example of a wild strange attractor," Mat. Sb. **189**, 137–160 (1998).

16 A. S. Gonchenko and S. Gonchenko, "Variety of strange pseudohyperbolic attractors in three-dimensional generalized Hénon maps," Phys. D 337, 43-57

¹⁷S. Gonchenko, C. Simo, and A. Vieiro, "Richness of dynamics and global bifurcations in systems with a homoclinic figure-eight," Nonlinearity **26**, 621–678 (2012)

¹⁸S. V. Gonchenko and I. Ovsyannikov, "Homoclinic tangencies to resonant saddles and discrete Lorenz attractors," Discrete Contin. Dyn. Syst. S **10**, 273–288 (2017).

¹⁹ A. S. Gonchenko, M. S. Gonchenko, A. D. Kozlov, and E. A. Samylina, "On scenarios of the onset of homoclinic attractors in three-dimensional non-orientable maps," Chaos 31, 043122 (2021).

²⁰M. Zhao, C. Li, J. Wang, and Z. Feng, "Bifurcation analysis of the three-dimensional Hénon map," Discrete Contin. Dyn. Syst. S **10**, 625–645 (2017)

²¹H. Richter, "The generalized Hénon maps: Examples for higher-dimensional chaos," Int. J. Bifurcation Chaos 12, 1371–1384 (2002).

²²S. Gonchenko, A. Gonchenko, A. Kazakov, and E. Samylina, "On discrete Lorenz-like attractors," Chaos **31**, 023117 (2021).

²³ A. Gonchenko, S. V. Gonchenko, A. Kazakov, and D. Turaev, "Simple scenarios of onset of chaos in three-dimensional maps," Int. J. Bifurcation Chaos 24, 1440005 (2014).

²⁴ A. Gonchenko, S. Gonchenko, and D. Turaev, "Doubling of invariant curves and chaos in three-dimensional diffeomorphisms," Chaos **31**, 113130 (2021).

- $^{\mathbf{25}}\mathrm{X}.$ Zhang, "Chaotic polynomial maps," Int. J. Bifurcation Chaos $\mathbf{26},\ 1650131$
- (2016).

 26Y. Kuznetsov and H. Meijer, Numerical Bifurcation Analysis of Maps (Cambridge University Press, Cambridge, 2019), Vol. 34. ²⁷J. Gallas, "Dissecting shrimps: Results for some one-dimensional physical
- models," Phys. A **202**, 196–223 (1994).

 ²⁸ R. MacKay and C. Tresser, "Some flesh on the skeleton: The bifurcation structure of bimodal maps," Physica D 27, 412–422 (1987).
- 29 W. Façanha, B. Oldeman, and L. Glass, "Bifurcation structures in twodimensional maps: The endoskeletons of shrimps," Phys. Lett. A 377, 1264-1268
- (2013). $$^{30}{\rm J.\,D.\,Meiss}$ and E. Sander, "Birkhoff averages and the breakdown of invariant
- tori in volume-preserving maps," Physica D **428**, 133048 (2021).

 ³¹H. Broer, C. Simó, and R. Vitolo, "Hopf-saddle-node bifurcation for fixed points of 3D-diffeomorphisms: Analysis of a resonance "bubble"," Physica D 237, 1773–1799 (2008).